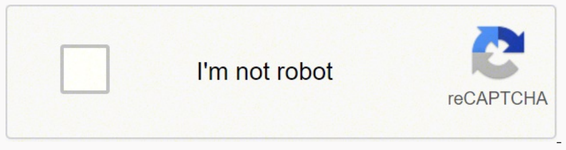

Continue

336840094.16667 10144180.142857 42147621032 3291476.6904762 12266139.606061 57663204.090909 18371946.29 46926966 22601923.505747 158028185562 13545864792 22167353.685714 5397583 875435816 110843398376 52163549.166667 9462917.9587629 27126014060 26382251336 2852673760 124255467000 94563985.411765 103112112.85 553951136

Camera calibration chessboard pdf online test download pc

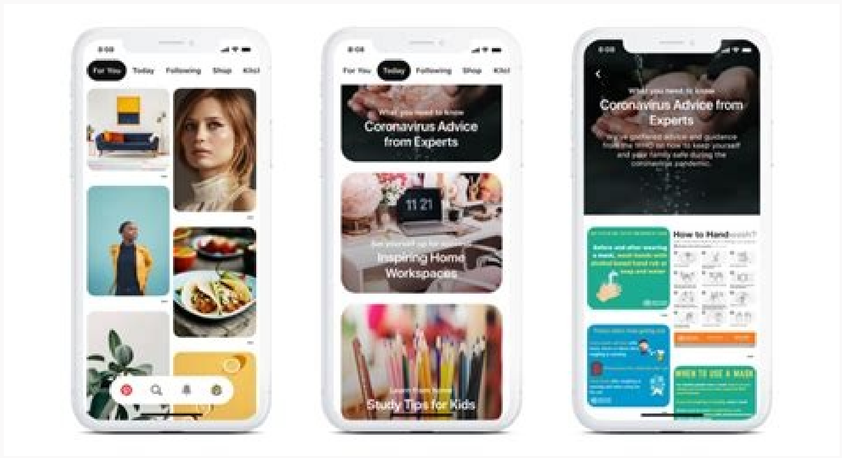

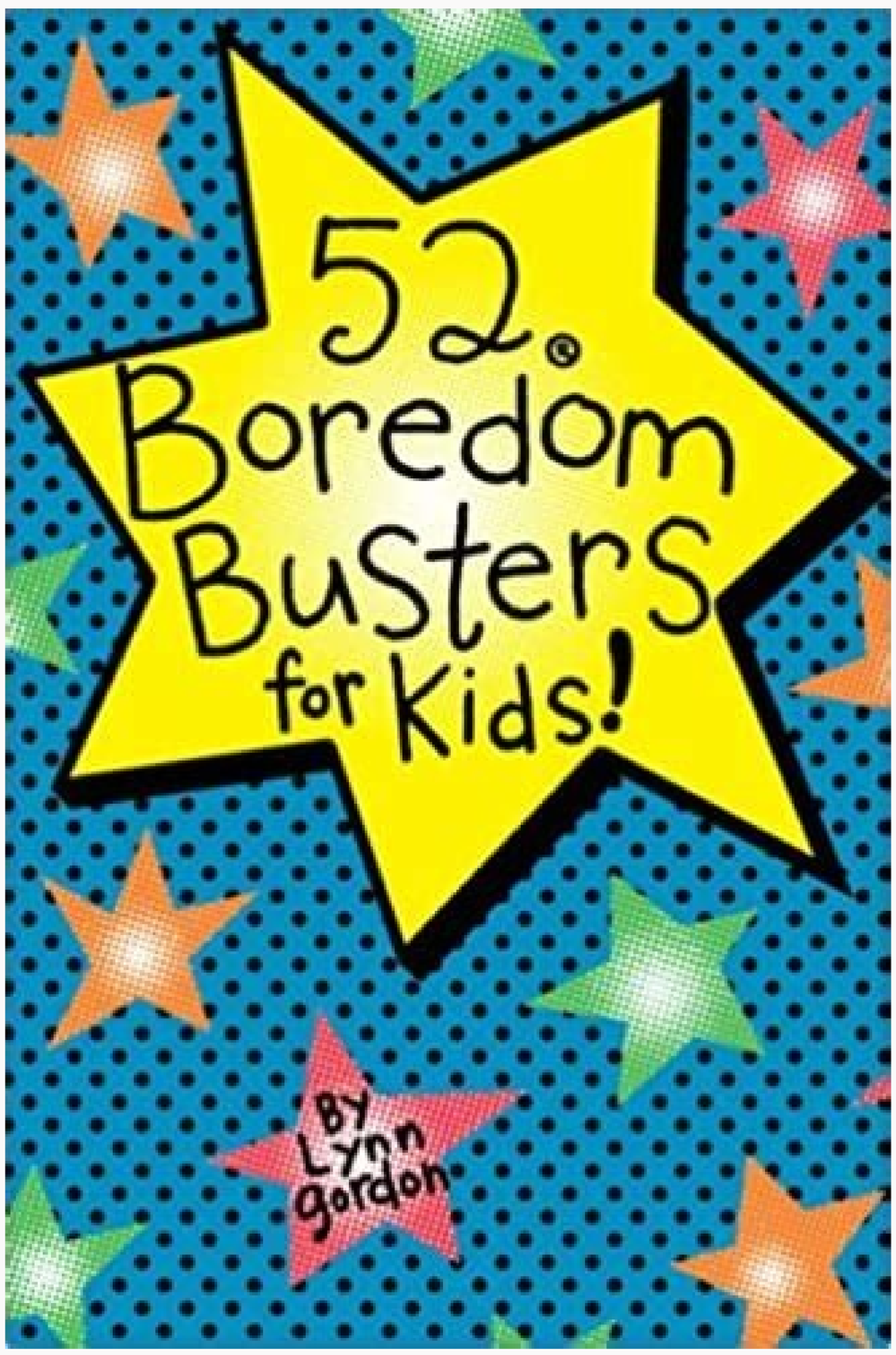

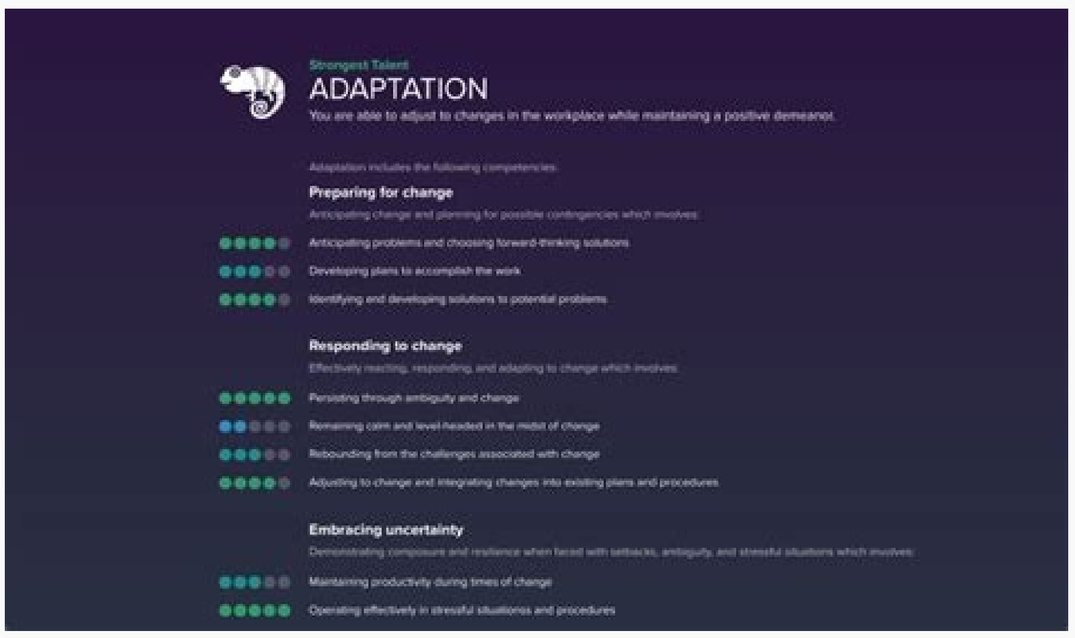

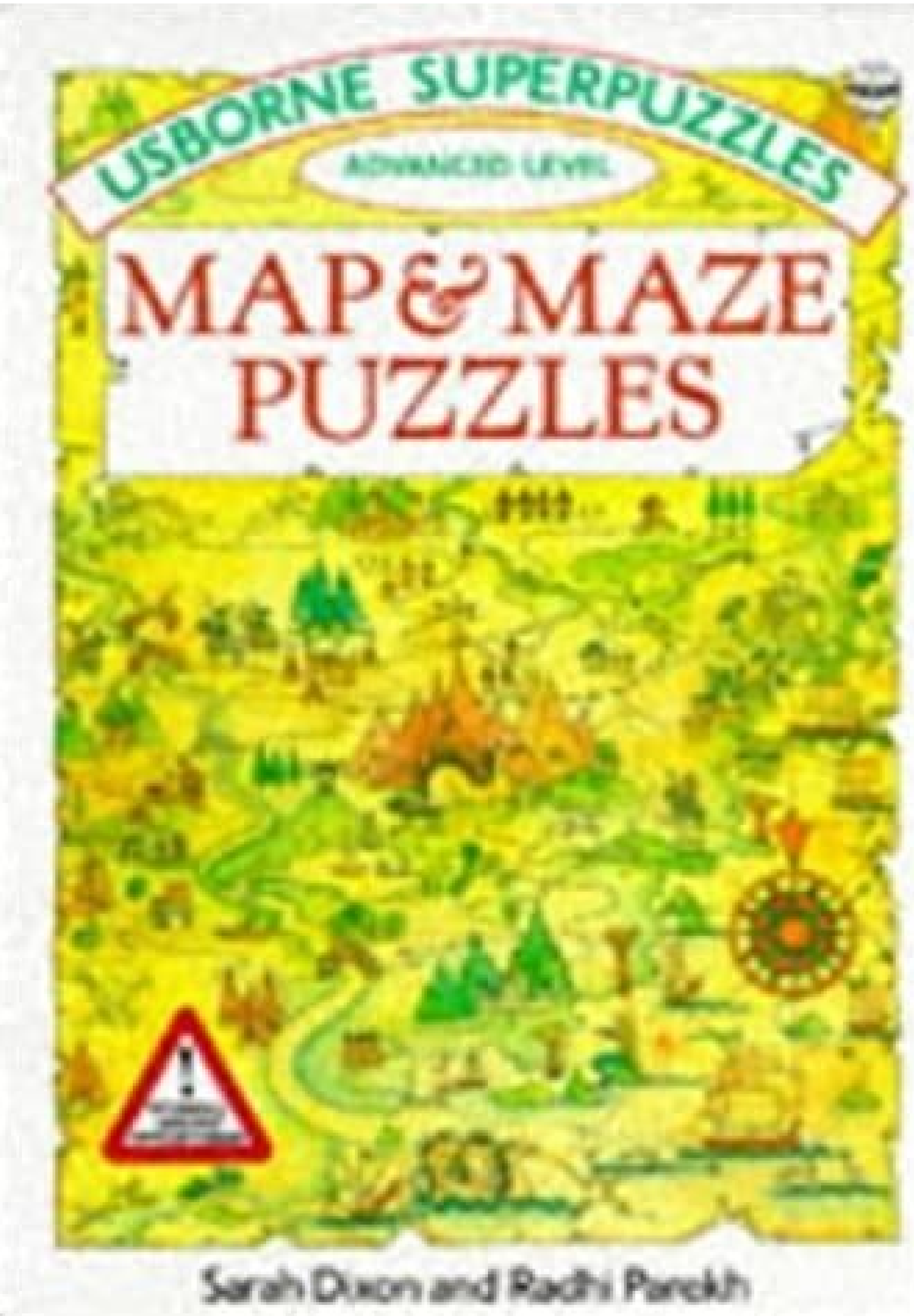

Tibaldi, M. Craford, “Status and future of high-power light-emitting diodes for solid-state lighting,” J. Download Full Size | PPT Slide | PDF It shows that when $\sigma _g=\sigma _w$, ${\partial Lc}/{\partial \sigma _g}=0$, which means Lc reaches the maximum at the best scale. Opt. Gu, A. 44(2), 185–191 (2008). Schnick, “A revolution in lighting,” Nat. (a) Chessboard target out of focus whose feature point is severely blurred and hard to be extracted accurately. 126, 105919 (2020). (f) RMSE of k_2. Callsen, B. For large-field-of-view cameras, it is hard to balance target size and image clarity: large targets that match field-of-view in the DoF range have relatively low accuracy, are difficult to manufacture, and are inconvenient to move and place; small- and medium-sized targets take up small coverage in image when put in the DoF range, but defocus blur will occur when they are put out of the DoF for large coverage. With the proposed method, the use of a small target in the non-DoF range for calibration can achieve the same effect as that using a large target in the DoF range. 98(16), 161107 (2011). Hu, and H. also reported an increase in C with increasing temperature in an InGaN single QW structure: a ~35% increase in C from 25 to 100°C [18]. This inhomogeneity in hole distribution resulted from inefficient hole transport through QWs caused by low hole mobility. Wang, and C. Rep. From the EQE and IQE data in Figs. 1 and 2, the light extraction efficiency (LEE), which is defined as the ratio of EQE to IQE, was obtained to be ~0.83. Because the mean of the feature points’ location errors is generally assumed to be 0, the standard deviation of feature point locations is basically equal to the root mean square error (RMSE) of those in value. Shim, “Rate equation analysis of efficiency droop in InGaN light-emitting diodes,” Appl. Rafailov, “Temperature-dependent internal quantum efficiency of blue high-brightness light-emitting diodes,” IEEE J. Binder, M. Craven, “Thermal droop in high-quality InGaN LEDs,” Appl. [19] established a regional description of point uncertainty area to optimize the image coordinates of target feature points together with camera parameters. Yi, and G. Baur, M. Y. [CrossRef] 48. + n.$, and $\tilde {I}.. Wang, B. (Left) Small target calibration scenario. Mueller, L. (Middle) Small chessboard target. Yapparov, L. Equations on this page are rendered with MathJax. J. Hooker and E. In this study, to clarify this issue, the temperature dependence of C was investigated by fitting the EQE data of an InGaN blue MQW LED using an analytical model or numerical simulation. [CrossRef] 24. Yuh, Y. Manik, and A. Mukunoki, and N. For the simulation, we employed a commercial software, APSYS, which self-consistently solves the QW band structures, radiative and nonradiative carrier recombination, and the drift and diffusion equation of the carriers [34]. (Middle) Large target calibration scenario. Alert me when this article is cited. Das, V. Figure 9 shows distributions of re-projection errors of different calibration methods. Fig. Schmidt, and W. 20 images are generated for calibration with 36 feature points per image, and the distance between adjacent points is 8 mm. Ryu, Y. Sone, S. Wagner, “Influence of indium content and temperature on Auger-like recombination in InGaN quantum wells grown on (111) silicon substrates,” Appl. [18] showed that blur width can be calculated through the lens diameter and front DoF and that the blur can be considered as a calibration parameter in calibration and optimization processes. Optica participates in Crossref's Cited-By Linking service. Zhu, and A. Calibration targets in focus or out of focus. 9. At 20°C, the distribution of hole concentration is quite inhomogeneous, decreasing rapidly as hole carriers move from the p-side to the n-side QW. [CrossRef] 17. As the temperature was increased from 20 to 100°C, A(T) increased from 8.7 × 106 to 12.7 × 106 s−1 and C(T) decreased from 3.51 × 10−29 to 3.38 × 10−29 cm6/s. Goano, G. Li, P. The light output power (LOP) was measured as the injection current increased up to 350 mA for each temperature. Therefore, Eq. (10) can be simplified as (11)$$\begin{aligned} & {{s}_{0}}=\frac{{{n}_{s}}\left({{f}_{st}}-{{f}_{tt}} \right)}{{{f}_{ss}}{{f}_{tt}}-f_{st}^{2}}=-\frac{{{n}_{s}}}{{{f}_{ss}}}, \\ & {{t}_{0}}=\frac{{{n}_{t}}\left({{f}_{st}}-{{f}_{ss}} \right)}{{{f}_{ss}}{{f}_{tt}}-f_{st}^{2}}=-\frac{{{n}_{t}}}{{{f}_{tt}}}. Nakamura, S. Moreover, the proposed method has a higher accuracy than directly applying Zhang’s method when the location variances of the feature points differ. Also, the accuracy of the proposed method approaches to that of LZ which is the benchmark. G. Gool, “Stratified self-calibration with the modulus constraint,” IEEE Trans. The figure shows good agreement between the calculated data and the fitted curve. (8) b P A R n = ∫ 400 700 (t g E d 0 + (λ)) e − K d (λ) z d λ (12) b P A R d = 2 ∗ ∫ ϕ r i s e ϕ n o o n ∫ 400 700 (t g E d 0 + (λ , θ s o l z ′ (ϕ)) e − K d (λ) z d ϕ d λ (13) ϕ r i s e = cos − 1 (− tan (δ) tan (l a t)) . In the numerical simulations, however, the inhomogeneous carrier distribution in MQWs was included when obtaining the temperature dependence of C. Kweon, “Accurate camera calibration robust to defocus using a smartphone,” in Proc. However, the increase rate of A was ~28% in the temperature range from 20 to 100°C, which was somewhat lower than those obtained in Fig. 4(a). 15(12), 125006 (2013). [CrossRef] 40. 11. [CrossRef] 16. Yan, D. 3(4), 323–344 (1987). Kioupakis, Q. Because in Tsai’s method, the principal point needs to be calibrated in advance and the definition of distortion coefficients is different from the proposed method, the focal lengths are mainly analyzed. Electron Devices 48(3), 535–542 (2001). = f. [18] and Refs. Differentiating Eq. (12) with respect to $\sigma _g^{2}$ and setting it as 0 yields (14)$$\frac{\partial \sigma _{{{s}_{0}}}^{2}}{\partial \sigma _{g}^{2}}=A\frac{2\left(\sigma _{g}^{2}-\sigma _{w}^{2} \right)}{{\left(\sigma _{g}^{2}+\sigma _{w}^{2} \right)}^{3}}}{\sigma _{g}^{6}}=0,$$ where $A={\sigma _{n}^{2}}/{\left (8\pi {{K}^{2}}\sigma _{w}^{4} \right)}$. 122(23), 234505 (2017). Section 6 covers the conclusions drawn.2. Mathematical model of cameraIn this study, the pinhole camera model and the Brown distortion model [20] are adopted.For a feature point Q, $\boldsymbol {q}=\left [x, y, z, 1\right]^\textrm {T}$ is the 3D homogeneous coordinate in the world reference frame. Brown, “Close-range camera calibration,” Photogramm. Li, J. Combining with the characteristic of variance, the location variance of the spot center is $\sigma _{{{s}_{0}}}^{2}=\sigma _{{{t}_{0}}}^{2}={\hat {\sigma }_{n}^{2}}/{{{f}_{ss}}^{2}}$.Therefore, the location variance of the light-spot center is (12)$$\sigma^2_{s_0}=\sigma^2_{t_0}=\frac{(\sigma^2_g+\sigma^2_w)^4}{8\pi\sigma^4_w\sigma^4_g}\left(\frac{\sigma^2_n}{K^2}\right).$$ When $\sigma _g$ = $\sigma _w$, Eq. (12) can be simplified as (13)$$\sigma _{{{s}_{0}}}^{2}=\sigma _{{{t}_{0}}}^{2}=\frac{2}{\pi }\left(\frac{\sigma _{n}^{2}}{{{K}^{2}}} \right),$$ where $\sigma _{n}^{2}$ is the variance of image noise $n\left (s, t\right)$, which can be estimated by the method in [25], and K is the maximum gray value in the vicinity of the light-spot center.Based on the model, it will be proved that when $\sigma _g=\sigma _w$, the location accuracy is the highest. SPIE 8262, 82620E (2012). Meneghini, F. Yang and Y. Jeong, J. Meneghini, C. Figure 11 shows that the error distribution of OURS is the most concentrated and closest to zero among the defocused camera calibration methods. 1. 121(5), 053105 (2017). Here, δ of 1.24 was obtained. Then, the LED package was soldered on a copper block with a temperature controlled by a thermo-electric cooler (TEC).The optical characteristics were measured using an LED characterization system with a calibrated integrating sphere when the TEC temperature was varied from 20 to 100°C. Re-projection errors of different calibration methods. Flory and G. 115(22), 223502 (2019). Pheng, “An efficient statistical method for image noise level estimation,” in Proc. [CrossRef] 2. Zeng, “Improved hole distribution in InGaN light-emitting diodes with InGaN-GaN barriers of decreasing indium composition,” Phys. Gu, and D. Watson, R. Here, three cases of temperature dependent B(T) were considered: the theoretical B(T) in Fig. 2 and the B(T) following the inverse power law dependence with δ equal to 1 and 1.5. A(T) was found to increase with increasing temperature for all three cases, as expected. It is important to understand the mechanisms of thermal droop and current droop of InGaN LEDs for their use in high-power and temperature-stable lighting applications. The fabricated LED chip was encapsulated with epoxy resin and mounted in a ceramic package as a type of surface-mount device. Hader, J. Choi, G. [CrossRef] 5. This increasing rate is slightly lower than the experimental result in the InGaN single QW structure [18] and approximately double the theoretically calculated one based on indirect Auger processes assisted by phonon coupling and alloy scattering [14,17]. As the temperature increases, this difference in C will be reduced because the effective active volume approaches the physical volume. In numerical simulation, on the contrary, the separation of electron-hole wavefunctions and the inhomogeneous carrier distribution were considered, which resulted in significant reduction in effective active volume and hence the larger value of C [52–55]. (b) The same as for (a) except log-log scaled scatterplots are of satellite-derived daily-integrated benthic PAR (bPARd) vs. q, h, and c are the elementary charge, Planck constant, and the speed of light in vacuum, respectively.Figure 1 presents the EQE determined using Eq. (1) as a function of the injection current up to 350 mA at temperatures of 20, 40, 60, 80, and 100°C. 14(5), 454–458 (2015). ${\boldsymbol {p}_{u}}={{\left [{{u}_{u}},{{v}_{u}},1 \right]}^\textrm {T}}$ and ${\boldsymbol {p}_{d}}={{\left [{{u}_{d}},{{v}_{d}},1 \right]}^\textrm {T}}$ are the undistorted and distorted homogeneous coordinates in the image reference frame in pixels, and the pinhole camera model can be described as (1)$$\rho {\boldsymbol{p}_{u}}=\boldsymbol{K}\left[\begin{matrix} \begin{matrix} 1 & 0 & 0 & 0 \\ \end{matrix} \\ \begin{matrix} 0 & 1 & 0 & 0 \\ \end{matrix} \\ \begin{matrix} 0 & 0 & 1 & 0 \\ \end{matrix} \\ \end{matrix} \right]\left[\begin{matrix} \boldsymbol{R} & \boldsymbol{t} \\ 0 & 1 \\ \end{matrix} \right]\boldsymbol{q},$$ where ρ is an arbitrary non-zero scale factor; $\boldsymbol {K}=\left [\begin {matrix} {{f}_{x}} & \gamma & {{u}_{0}} \\ 0 & {{f}_{y}} & {{v}_{0}} \\ 0 & 0 & 1 \\ \end {matrix} \right]$, f_x and f_y are the effective focal lengths in the direction of the u- and v-axes, respectively; u_0 and v_0 are the coordinates of the principal point; γ is the non-perpendicular between u- and v-axes; $\boldsymbol {R}=\left [{\boldsymbol {r}_{1}}, {\boldsymbol {r}_{2}}, {\boldsymbol {r}_{3}}\right]$ and $\boldsymbol {t}$ are the rotation matrix and translation vector that relate the world reference frame to the camera reference frame.According to [1,3,21], the first two order radial coefficients of the Brown distortion model are enough to describe distortion. DenBaars, and J. Meneghini, M. Mihopoulos, and M. Zhao, D. In addition, OURS performs the best among the four methods using the light-spot target, followed by GS, GF, and CT. = f.. Cho, E. In addition, the coefficient C increased by 31.4% over this temperature range. All of those prove the effectiveness of the proposed method.5.2.2 Analysis of the evaluation results using target images in the non-DoF rangeIn the non-DoF range, the small light-spot target used for calibration is used for evaluation with 14 poses different from calibration dataset,whose longest distance between a pair of points is 40 mm in each row or column and there are totally 168 pairs of point. This suggests that the descending behaviors of C with temperature in Ref. Lund, and M. Metrics [CrossRef] 39. Comparison of calibration scenarios of small target and large target. 69(8), 1286–1289 (2016). F. In semiconductors, A and C generally increase and B decreases with increasing temperature, leading to a decrease in efficiency with increasing temperature. Verzellesi, D. APSYS by Crosslight Software, Inc., Burnaby, Canada, Available: . At 100°C, where carrier recombination rates among QWs are reasonably uniform, the effective active volume of MQWs is expected to be similar to the physical volume of MQWs. That is, the effective active volume increases with increasing temperature. R. Simulated calibration results of the proposed method using 3D and 2D targets with increasing noise level. Bouguet, “The matlab open source calibration toolbox,” . Park, J. For completeness, the evaluation points are extracted by four methods: centroid method (named as IMG_CT), Gaussian fitting method (named as IMG_GF), Hessian method (named as IMG_GS), and the adaptive multi-scale method (named as IMG_MS, adopted in the proposed calibration procedure). 22(10), 1066–1077 (2000). Thus, it may be a better choice to calibrate a camera with 2D targets.5. Physical experimentThe effectiveness of the proposed method is also verified via physical experiments in which different calibration methods are evaluated by the calibration results of the intrinsic parameters and binocular measurements. (a) Relative RMSE of f_x. [CrossRef] 49. Magno-Canto, L. Affected by various conditions, the intensity distribution of the light spot is not strictly regularly Gaussian in the actual process of extraction of the feature points, and therefore, CT and GF perform worse. The red-yellow-green-magenta color scale represents month of observation. Experiments prove that the accuracy of the proposed method is comparable to that of Zhang’s method using large targets in the depth-of-field range. Download Full Size | PPT Slide | PDF Fig. As shown in Fig. 1(a), defocus causes severe blur to feature points of a chessboard target, which will lead to a decrease in the accuracy of extraction and calibration in traditional methods. Geograph. At 20°C, the ratio of the highest RAuger at the 5th QW (nearest p-GaN) to the lowest RAuger at the 1st QW (nearest n-GaN) was as large as 40. U. Vis. 100(8), 081106 (2012). Yadav, V. High-accuracy calibration is achieved through blurred images of small targets, which are placed in the non-depth-of-field range of cameras. Seo, and H. The properly determined temperature-dependent C is also expected to provide insight into the Auger recombination mechanisms in InGaN materials.National Research Foundation of Korea (NRF-2016R1D1A1B03932092, NRF-2019R1A2C1010160); Korea Institute of Science and Technology (2E30100-20-038).AcknowledgmentsThis work was supported by the National Research Foundation of Korea (NRF) grant funded by the Ministry of Science and ICT (NRF-2019R1A2C1010160) and the Ministry of Education (NRF-2016R1D1A1B03932092), and by the KIST Institutional Program (2E30100-20-038).DisclosuresThe authors declare no conflicts of interest.References1. Algorithm procedure. Koch, “Temperature-dependence of the internal efficiency droop in GaN-based diodes,” Appl. Lee, “A comparative study of efficiency droop and internal electric field for InGaN blue light-emitting diodes on silicon and sapphire substrates,” Sci. These methods solve the problem of defocus blur to some extent but the location accuracy of feature points in cases of severe blur remains low.The third method establishes a blur model, to overcome the effect of defocus blur [18,19]. Albrecht, and P. Moreover, the carrier distribution in MQWs could be strongly dependent on the temperature as a result of thermally enhanced carrier transport through the MQW layers [31–33]. Pan, “Camera calibration using synthetic random speckle pattern and digital image correlation,” Opt. Froehlich, W. Based on the above analysis, a high-accuracy calibration method of cameras without DoF and target size limitations is proposed, which explicitly deals with defocus blur and image noise. The carrier density n is also assumed to be constant through all QW layers. 127(21), 211102 (2020). B. Zerova, M. Zulonas, B. That means overall the 3D target has slightly higher accuracy than the 2D target for the proposed method, but it easily suffers from self-occlusion and limited number of feature points. Piprek, “Efficiency droop in nitride-based light-emitting diodes,” Phys. Therefore, the temperature dependence of C can be determined correctly when the temperature-dependent redistribution of carriers in MQWs is considered. Moreover, there are three types of targets: (1) a large chessboard target whose interval of adjacent points is 20 mm with a total of 6×6 feature points placed in the DoF range and extracted by the Harris method [28] (LZ); (2) a small chessboard target whose interval of adjacent points is 5 mm with a total of 6×6 feature points placed in the non-DoF range and extracted by the Harris method (SZ), and (3) a light-spot target whose interval of adjacent points is 8 mm with a total of 6×6 feature points placed in the non-DoF range and extracted by the proposed method (OURS), Hessian method [29] (GS), Gauss fitting method [30] (GF), and centroid method [30] (CT), respectively. 31(2), 376–383 (2009). Finally, the high-accuracy intrinsic and extrinsic parameters of the camera under test are obtained by nonlinear optimization where re-projection errors are normalized by location variances according to the Gauss-Markov theorem. 15 (Citeseer, 1988), pp. Krames, “Carrier distribution in (2008)InGaN/GaN multiple quantum well light-emitting diodes,” Appl. [CrossRef] 29. (b) Feature point image coordinate extraction method and location variance estimation method. [19–23] could be due to the assumption of a constant carrier density through MQWs independent of temperature.In this study, we investigate the temperature dependence of the Auger recombination coefficient in an InGaN/GaN blue MQW LED structure considering the temperature-dependent carrier distribution in MQWs. The external quantum efficiency (EQE) of the LED sample was measured as temperatures between 20 and 100°C. From this point, traditional methods can be regarded as the special case of the proposed method.Binocular stereo vision sensors can be calibrated by the proposed method combined with the method introduced in [27].4. The above analysis shows that the proposed method can still achieve high-accuracy measurement in the DoF range, although calibrated in the non-DoF range, which approaches to the accuracy of the focused camera calibration method (LZ); moreover, the proposed method behaves the best among defocused calibration methods. Inform. Based on that, location variance of each feature point is specifically estimated, and is used to normalize re-projection errors during non-linear optimization to obtain optimal solution according to the Gauss-Markov theorem. The small rectangle inside represents the mean value. Fig. Fleetwood, “Temperature-dependent efficiency droop in GaN-based blue LEDs,” IEEE Electron Device Lett. As previously reported, bias and MAE were smaller in clearer offshore waters (Palm Passage and Myrmidon) compared to more optically complex inshore (Yongala) and midshelf (Heron) waters. Ryu, G. 239–250.Page 2Over the last two decades, there has been remarkable progress in the development of InGaN/GaN-based light-emitting diodes (LEDs) for use in solid-state lighting and display applications owing to their high efficiency and eco-friendliness [1–3]. \\ \end{aligned}$$The ideal image, noise, and convolutional kernel satisfy a Gaussian distribution, resulting in $n_s=n_t$. La Grassa, B. Deb, O. Rinke, K. 101(13), 131111 (2012). [CrossRef] 36. 147–151.29. Zanoni, “Efficiency droop in InGaN/GaN blue light-emitting diodes: Physical mechanisms and remedies,” J. [CrossRef] 27. Intrinsic parameters of the cameras under test are calibrated by the above listed methods, respectively, and the structure parameters are calibrated by taking the calibration target as the intermediary [22]. Bellotti, K. Tehrani [17] configured an extremely small pore plate in front of a lens to form a light-spot target, to reduce the impact of defocus blur. Bertazzi, D. Moreover, the estimated standard deviation of location, $\sigma _{s_0}$, is basically consistent with $\sigma _e$, which proves the above derivation. Moreover, the mechanism for this counter-intuitive temperature dependence of C has not been clearly understood.Experimentally, the recombination coefficients in the QW active region have usually been obtained by fitting the measured efficiency as a function of current using the ABC recombination model [18–23]. [CrossRef] 9. Harbers, and M. N. Park, “Extraction of recombination coefficients and internal quantum efficiency of GaN-based light emitting diodes considering effective volume of active region,” Opt. Ghillino, G. Figure 7 shows the electron and hole concentration distribution in five InGaN QWs at temperatures 20, 60, and 100°C when the injection current was 100 mA. Therefore, the experimentally extracted recombination coefficients based on the ABC model with a constant carrier density could deviate significantly from the actual values. Ryu, H. [CrossRef] 22. And for a shallow-DoF camera, its DoF is limited and defocus blur occurs easily during calibration. Choi, and B. The targets are commercial available, and the targets used here are ordered at . Applying the Arrhenius model (${\propto} \exp [- {E_a}/{k_B}T]$) with an activation energy Ea to A(T) in Fig. 4(a), Ea of 41 to 48 meV was obtained. \end{array}$$ Note that the coefficients a, b, and c have no explicit dependence on A, B, C, and V. Liu, Q. Ha, “Effect of active-layer structures on temperature characteristics of InGaN blue laser diodes,” Opt. Photon. Ryu and K. Ryu, K. These methods consider blur only and ignore image noise. Good agreements between the measured data and the fit curves are observed for all temperatures. (b) Relative RMSE of f_y. Error distributions of different calibration methods evaluated by different evaluation point coordinates in the non-DoF range. Zhao, H. Piprek, “AlGaN polarization doping effects on the efficiency of blue LEDs,” Proc. Moreover, the calibration results of the light-spot target are better than those of the chessboard target among methods performed in the non-DoF range, which proves the advantage of the light spot in defocused camera calibration. Zhang, and Z. Evaluation images. Express 22(2), 1235–1242 (2014). 17(10), 1298–1302 (2017). Spinger, P. Short, “Comparison of some techniques for the subpixel location of discrete target images,” in Videometrics III, vol. Garetto, E. 9(19), 4160 (2019). Asada, “A unified camera calibration using geometry and blur of feature points,” in International Conference on Pattern Recognition, (2006).19. 109(2), 021104 (2016). [CrossRef] 38. Moreover, the center of radial distortion is assumed to be the same as the principal point here. The calibration method of 3D target is Tsai’s method [1] with normalization (named as 3D) where the proposed method can be easily applied and the re-projection errors in the non-linear optimization are normalized. In addition, the temperature dependence of A could not be fitted well to the Arrhenius model in this case, which was attributed to the temperature-dependent carrier distribution in InGaN MQWs.As shown in Fig. 6(b), the coefficient C also increased steadily from 2.07 × 10−30 to 2.72 × 10−30 cm6/s with increasing temperature from 20 to 100°C. Figure 4 presents the simulation results showing that with a increasing noise level, the standard deviation of location, $\sigma _e$, continues to be essentially equal to the RMSE of location. This opposite temperature dependence in C between two methods was attributed to the temperature-dependent carrier distribution in InGaN MQWs. As the temperature increases, the carrier distribution in MQWs becomes increasingly homogeneous. Pust, P. 100(13), 131109 (2012). This large difference in C values resulted from the fact that the analytical ABC model assumed the carrier density is constant inside a QW and uniform throughout MQW layers. Galler, T. At a certain scale, the center of the light spot is determined by calculating the extreme value of C. (d) Calculation of camera intrinsic and extrinsic parameters. Zhang, “Camera calibration with one-dimensional objects,” IEEE Trans. Ghione, J. The electron concentration did not change significantly with temperature. Kure, C. Each rectangle represents the measurement error of a calibration method. Yin, “The effects of temperature on optical properties of InGaN/GaN multiple quantum well light-emitting diodes,” J. Li, Y. Tehrani, T. Therefore, it is important to propose a camera calibration method that is not limited by DoF and target size. Fig. The structure parameters calculated by different methods are listed in Table 3, where $\boldsymbol {om}$ is the rotation vector which can derive rotation matrix $\boldsymbol {R}$ by rodrigues transform. Maybank, “Camera self-calibration: Theory and experiments,” in Proc. Intell. Zhang, M. Park and Y. Wang, and S. Mij denotes the momentum matrix element, and fi and fj represent the Fermi functions for the conduction and valence band, respectively. Only the left top 6×6 points are used for both chessboard targets. In many cases, the reported δ values of the InGaN QW LEDs have been between 1.0 and 1.5 [19–21,42]. Because LZ performs Zhang’s method in the DoF range, which is popular and state-of-the-art, it is set as the benchmark. Fig. 99(17), 171106 (2011). Chen and B. Götz, “Progress in high-luminance LED technology for solid-state lighting,” Phys. This is because the feature points with a larger location variance have a lower location accuracy. The results are shown in Fig. 5. Fig. Bok, K. 4. That is, B(T) in Fig. 3 was used. RMSEs of the camera parameters with increasing location noise. Lu, H. M. Jeon, M. When the theoretical data of B(T) in Fig. 3 were used, C(T) decreased steadily by ~12% in the temperature range of 20 to 100°C. 22(11), 1330–1334 (2000). First, a high-accuracy light-spot small target is placed closely in front of the camera, so that the target image can take up a large proportion in the whole image. These methods can realize camera calibration under defocus blur. [CrossRef] 14. Kim, and E. of European Conference on Computer Vision, (1992).9. ${\boldsymbol {p}_{d,ij}}$ is the distorted coordinate in the image reference frame of the i-th point in the j-th image, and ${{\tilde {\boldsymbol {p}}}_{d,ij}}$ is the distorted coordinate of the corresponding re-projection point.However, based on this study, location variances vary with points when there is defocus blur and large and uneven image noise. [CrossRef] 8. Beeler, and A. Steger, “An unbiased detector of curvilinear structures,” IEEE Trans. Franz, and J. [CrossRef] 20. Liu et al. The above analysis verifies the effectiveness of the proposed method.5.2 Evaluation of binocular measurement resultsThe goal of calibration is measurement, thus different calibration methods are evaluated objectively by binocular vision measurement in this section. 10. We note that these corrections did not affect the relevance of our results to understanding benthic light and its effects within the Great Barrier Reef World Heritage Area. Fig. During evaluation, a light-spot planar target is placed in the field-of-view of binocular cameras with different poses, providing pairs of points to be measured. Kang, Z. Zhu, “Camera calibration with moving one-dimensional objects,” Pattern Recognit. The calculated B(T) was fitted with the inverse power law, which is shown as the dotted line in Fig. 3. Here, $E_d^{{0^ + }}$is the above-water downwelling plane solar irradiance, F0 is the extraterrestrial solar irradiance, T is a transmittance parameter that accounts for atmospheric absorption and scattering by gases, clouds, and aerosols [2], and θ′solz(ϕ) is the solar zenith angle at a given time between sunrise to noon at each hour angle $\phi $. Instrum. Status Solidi A 207(10), 2217–2225 (2010). Goano, S. 8. Automat. We notice that Refs. The peak emission wavelength was ~450 nm at 20°C. Galler, P. Kuo, Y. Korean Phys. Deng, M. Zanoni, “Role of defects in the thermal droop of InGaN-based light emitting diodes,” J. In addition, when adjusting the brightness of the light-spot target, one should turn it down appropriately to maintain the Gaussian distribution of the spot when target is in focus; and turn it up relatively when the target is out of focus to conquer the decrease of brightness caused by defocus. Fig. Laubsch, M. Express 27(20), A1350–A1371 (2019). (d) Relative RMSE of v_0. (a)-(d) are methods evaluated by IMG_GF, IMG_CT, IMG_GS, and IMG_MS, respectively. Liu, and X. Soer, P. (b) Light-spot target in focus. 21(8), 707–724 (1999). 12. Sci. Yang, H. Ha, Y. Kim, J. Herrnsdorf, S. The data in Fig. 6(b) could not be fitted with the Arrhenius model well, implying that the direct band-to-band Auger recombination mechanism may be excluded. Young, C. However, the majority of groups have shown experimentally that C showed decreasing behaviors with increasing temperature at least for temperatures higher than 300 K [19–23]. Download Full Size | PPT Slide | PDF From Table 4 and Fig. 11 it can be drawn that the measurement results of OURS approach to those of LZ when evaluated in the DoF range. As the temperature was increased, both recombination rates become increasingly homogeneous through the MQW layers. Kaeding, N. Scholars have conducted some research on this problem, whose methods can be classified into the following three types:The first type establishes phase shift structures to overcome defocus blur [12–14]. The MQW active layers were composed of five 3-nm-thick InGaN QWs separated by 8-nm-thick GaN barriers. The settings for the planar target are same as OURS in Section 4.1, and the setting of the noise level is also the same as Section 4.1. The experiment at each noise level repeats 100 times and the noise is re-added at each iteration. Download Full Size | PPT Slide | PDF Based on the above analysis, if high-accuracy calibration can be achieved by blurred images captured out of the DoF, the method breaks the limitations of DoF and target size. This theoretical IQE curve was compared with the measured EQE data at a given temperature, T. [19–23]. Wang, S. 188–210.25. Monavarian, S. Further theoretical and experimental studies on the temperature dependence of C are expected to reveal the mechanism of Auger recombination processes in the InGaN QW.Up to now, the temperature dependence of C in InGaN QWs has been reported to be inconsistent. And the longest distance in each row or column is 100 mm and there are totally 108 pairs of point. of IEEE International Conference on Computer Vision, (2015).16. For an ideal light-spot center, differentiating Eq. (7) with respect to $\sigma _g$ and setting it as 0, that is (15)$$\frac{\partial Lc}{\partial {{\sigma }_{g}}}=\frac{\partial \left({{\sigma }_{g}}^{4}\left({{f}_{ss}}{{f}_{tt}}-{{f}_{st}}^{2} \right) \right)}{\partial {{\sigma }_{g}}} = \frac{{{M}^{2}}}{4{{\pi }^{2}}}\frac{4\left(\sigma _{g}^{5}-\sigma _{g}^{3}\sigma _{w}^{2} \right)}{{\left(\sigma _{g}^{2}+\sigma _{w}^{2} \right)}^{5}}=0.$$ Fig. On the other hand, in the analytical model in Section 3.1, the volume V of the QW active region in Eqs. (2) and (6) was constant and independent of temperature. Download Full Size | PPT Slide | PDF 3.1 Adaptive multi-scale extraction method of light spot centerIdeally, the intensity distribution of a light spot obeys a symmetric two-dimensional Gaussian distribution, and it can be expressed as follows: (5)$$f(u,v)=\frac{M}{2\pi\sigma^2_w}exp\left(-\frac{u^2+v^2}{2\sigma^2_w}\right),$$ where $\sigma _w$ is the standard deviation of the light spot.Considering the influence of noise, the actual intensity distribution of the light spot, $I(u,v)$, can be expressed as $I(u,v)=f(u,v)+n(u,v)$, where $n\left (u,v\right)$ is the image noise with a mean of 0 and variance of $\sigma _{n}^{2}$.The Hessian matrix at any image feature point is (6)$$\boldsymbol{H}\left(u,v \right)=\left[\begin{matrix} {{{\tilde{I}}}_{uu}}\left(u,v \right) & {{{\tilde{I}}}_{uv}}\left(u,v \right) \\ {{{\tilde{I}}}_{uv}}\left(u,v \right) & {{{\tilde{I}}}_{vv}}\left(u,v \right) \\ \end{matrix} \right],$$ where ${{\tilde {I}}}_{uu}}\left (u,v \right)$, ${{\tilde {I}}_{uv}}\left (u,v \right)$, and ${{\tilde {I}}_{vv}}\left (u,v \right)$ refer to the images convoluted by second-order Gaussian differential operators. Schubert, S. 34(10), 2058–2064 (2012). Kuritzky, Y. The absence of electron leakage in the simulation of this study is consistent with the previous report using the similar simulation parameters [51]. Hua, G. Moreover, it is up to 41.7% higher than GS, which proves the effectiveness of the adaptive multi-scale extraction method and the normalized optimization method. As the temperature was increased from 20 to 100°C, the actual hole concentration in p-GaN was found to increase from 1.3 × 1017 to 3.3 × 1017 cm−3. Krames, O. Peretti, and J. [CrossRef] 34. Fu, G. That is, the present analytical model also showed a similar temperature dependence of C to those reported previously.In Fig. 4, the absolute values of coefficients A(T) and C(T) are also shown on the right axis of each figure. I. Hoffmann, “Temperature-dependent recombination coefficients in InGaN light-emitting diodes: Hole localization, Auger processes, and the green gap,” Appl. At 100°C, this ratio was reduced considerably to only ~2.The simulation results in Figs. 8 and 9 show that the carrier recombination occurs mainly at the 5th QW nearest the p-side layers at 20°C. Meas. The EQE is determined using the following formula [32]: (1)$$\textrm{EQE} = \frac{{q{\lambda _c}}}{{hc}}\frac{{P{}_{\textrm{out}}}}{I},$$ where λc is the centroid wavelength of an emission spectrum, Pout is LOP, and I is current injected into the LED sample. By integrating rsp(ω), the radiative recombination rate Bn2 is calculated and the coefficient B is then obtained. Zhu, J. 38(9), 1446–1448 (2013). At 20°C, the distributions of both Rrad and RAuger were significantly inhomogeneous, decreasing rapidly from the p-side to the n-side QW. Steger, “Analytical and empirical performance evaluation of subpixel line and edge detection,” in Empirical Evaluation Methods in Computer vision (Los Alamitos, California, 1998), pp. By fitting the measured EQE curve with the IQE curve given by Eq. (5), ηp of the LED can be determined for each temperature.Figure 2 shows the IQE curves along with measured data at 20, 40, 60, 80, and 100°C. Lookman, and C. Martinelli, J. Comparison of standard deviation of actual location, $\sigma _e$, RMSE of actual location, $Erms$, and estimated standard deviation of location, $\sigma _{s_0}$, with increasing image noise. Janne, “Joint depth and color camera calibration with distortion correction,” IEEE Trans. [CrossRef] 47. As the temperature is elevated, more QW layers begin to act as an effective active region. [CrossRef] 11. By comparing the results obtained using these two methods, it is expected that the origin of the peculiar temperature dependence in C reported in previous works can be clarified, and the temperature-dependent C can be determined reliably.The epitaxial layers used for this study were grown on a c-plane sapphire substrate by metal-organic chemical vapor deposition. Eng. The IQE of an LED is defined as (3)$$\eta = \frac{{B{n^2}}}{{An + B{n^2} + C{n^3}}}.$$ In the IQE versus current relation, which is often referred to as the IQE curve, the peak IQE, ηp and the corresponding injection current, Ip are related to the coefficients A, B, and C as follows [35]: (4)$${\eta _p} = \frac{B}{{B + 2\sqrt {AC} }},\quad {I_p} = \frac{{qVA}}{C}(B + 2\sqrt {AC}).$$ Using Eqs. (2)–(4), the IQE curve can be obtained by solving the following quadratic equation on I [36]: (5)$$\begin{array}{c} \textrm{ }a{I^2} + bI + c = 0,\\ \textrm{where }a = \eta _{}^\textrm{3}\textrm{, } b = 2{\eta _p}{I_p}[\eta _{}^\textrm{2} - \frac{{2\eta _p^2{{(1 - \eta)}^2}}}{{{{(1 - {\eta _p})}^2}}}]\textrm{, }c = \eta \eta _p^2I_p^2. [CrossRef] L. If they are treated with the same weightage as the high-accuracy points in the optimization, the calibration results will be degraded. Zhang, B. Joo, J. 3(2), 160–175 (2007). Ryu, “Evaluation of the temperature-dependent internal quantum efficiency and the light-extraction efficiency in a GaN-based blue light-emitting diode by using a rate equation model,” J. H. Karpov, G. Thus, the pixel-wise coordinate at this scale is taken as the pixel-wise coordinate ${\boldsymbol {p}_{p}}={{\left [{{u}_{p}},{{v}_{p}} \right]}^\textrm {T}}$ of the feature point. Moreover, among the calibration methods performed in the non-DoF range, OURS achieves the highest accuracy up to 0.1528% for the same evaluation point, followed by GS, CT, GF and SZ. Notably, the corrections have led to a more consistent model bias and mean absolute error (MAE) across the test sites. [CrossRef] 7. In view of the above-mentioned problems, this study proposes a high-accuracy camera calibration method, which can overcome the influence of image blur and noise and is not limited by depth of field and target size. In fact, the synthetic standard deviation of OURS and SZ is about 1.58 times the noise level, which is higher than that of LZ. Marcinkevicius, R. The conventional ABC model assumes that the carrier density is constant through InGaN/GaN multiple-quantum-well (MQW) structures. Kim, C. Hafiz, M. C. Kang, H. Huang, Q. Lugauer, and E. Allsopp, M. Basu, “Influence of temperature on different optoelectronic characteristics of InGaN light emitting diodes,” Opt. Goano, “Thermal droop in III-nitride based light-emitting diodes: Physical origin and perspectives,” J. In $o-st$, the sub-pixel coordinate of the feature point is $\left (s_0, t_0\right)$. As δ smaller than 1 has not been reported, it can be regarded that the C(T) for δ = 1.0 is an upper-limit result, and hence, it can be regarded that C(T) decreased with increasing temperature overall. Goano, E. [18] and 54 meV in Ref. Can, S. 99(18), 181127 (2011). Baek, K. David, M. B was found to decrease from 0.663 × 10−10 to 0.49 × 10−10 cm3/s as the temperature was increased from 20 to 100°C.The temperature dependence of B has often been described as an inverse power law of the form 1/(Tδ) with the single exponent δ which can be simply expected to be 1.5 and 1.0 for the bulk and QW semiconductors, respectively [22,41]. Electron Devices 57(1), 79–87 (2010). Robot. And the results are show in Fig. 6. Fig. In this study, we found that the temperature dependence of C can be determined correctly when the temperature-dependent carrier distribution in MQWs is considered. Meneghesso, E. Ruden, “Monte Carlo simulation of electron transport in the III-nitride wurtzite phase materials system: binaries and ternaries,” IEEE Trans. Fabricius, “Model for deriving benthic irradiance in the Great Barrier Reef from MODIS satellite imagery,” Opt. In the analytical model, where the carrier density in InGaN MQWs was assumed to be constant independent of temperature, C decreased with increasing temperature, as in the case of previous experimental works on InGaN MQWs. On the other hand, the numerical simulation included the effects of an inhomogeneous carrier distribution in MQWs and its temperature-dependent redistribution. Galler, R. in situ daily bPAR. As to the carrier mobility, the mobility model and parameters of Refs. [CrossRef] 53. Finally, high-accuracy intrinsic and extrinsic parameters of the camera under test are obtained via normalized non-linear optimization, as depicted in Figs. 2(c) and (d). Fig. Ling, T. Download Full Size | PPT Slide | PDF As shown in Table 5, OURS achieves the highest accuracy up to 0.0403% for one certain kind of evaluation point. Figure 9 presents that re-projection errors of OURS are most concentrated among defocused camera calibration methods, whose standard deviation is 0.0406 pixel and approaches to that of LZ. This absolute value of C obtained by numerical simulation was found to be more than 10 times lower than that obtained by the analytical model in Fig. 4(b). (c) Light-spot target out of focus. Hopkins, D. [CrossRef] 30. Piprek, “How to decide between competing efficiency droop models for GaN-based light-emitting diodes,” Appl. Section 2 provides an overview of the camera model. This value almost corresponds to the median value of the reported range of δ in B.With the obtained information of ηp(T), Ip(T), and B(T), the temperature dependence of A and C were determined using Eqs. (7) and (8), respectively. The results of the camera calibration are listed in Table 1 and Table 2, where the values after plus or minus sign represent the uncertainties of the corresponding parameters, and the last column (repE) is the RMSE of the re-projection errors. Here, V is the product of the area of the QW planes and the total thickness of the MQW layers, and is assumed to be constant independent of temperature. Morkoç, “Improvement of carrier injection symmetry and quantum efficiency in InGaN light-emitting diodes with Mg delta-doped barriers,” Appl. Status Solidi A 212(8), 1805–1809 (2015). The IQE curve for a given temperature was simulated varying the coefficients A and C. Consequently, if the conventional ABC model with constant carrier density was employed, the temperature-dependent recombination coefficients would be determined incorrectly. Compared with traditional fixed target patterns with limited feature points, some methods use TFTs of panels [10,11] to complete calibration, whose feature points can be up to millions of points, and could achieve higher accuracy. Express 16(14), 10849–10857 (2008). The layer structure consisted of a Si-doped n-GaN layer, MQW active region, a 15-nm-thick p-type Mg-doped AlGaN electron-blocking layer, and 150-nm-thick Mg-doped p-GaN layer. Kelly, and M. This section will verify whether the proposed method has higher accuracy with 3D targets.Also, the coordinates of feature points are generated directly, and the 3D target composes of two orthogonal planes with 6$\times$6$\times$6 points, whose interval is 8mm. Shin, and J. Therefore, the minimum of $\sigma _{s_0}$ indicates the highest location accuracy. Z. Pietzonka, H. Piccardo, L. Cao, E. The experimental settings are as follows: f_x = f_y = 5000 pixel, u_0= 968.5 pixel, v_0= 728.5 pixel, and k_1 = k_2 = 0.05. The temperature dependence of A differs among samples because A depends on the quality of the active region. Kumar, A. Download Full Size | PPT Slide | PDF 1. Figure 10 presents pairs of points provided by one image used for evaluation. Zanoni, and M. Asundi, “Camera calibration with active phase target: improvement on feature detection and optimization,” Opt. Choi, and J. Piprek, Semiconductor Optoelectronic Devices

(Academic Press, 2003), Chap. Comput. (c) Normalization of location variances of the extracted coordinates. Faugeras, Q. Express 24(21), 24321–24336 (2016). Citing articles from Optica Publishing Group journals and other participating publishers are listed here. Wang, and H. V. Yellow lines indicate pair of points in each row, and blue lines represent pair of points in each column. Because the effective volume of MQWs at relatively low temperatures is much smaller than the physical volume V, the coefficient C could be overestimated if the physical volume of all MQW layers was used as V in Eq. (6). Lan, C. [12] projected sinusoidal phase shifting images in horizontal and vertical directions on a liquid crystal display (LCD) and determined the coordinates of the feature points. S. As a measure of the uniformity in the distribution, we calculated the coefficient of variation (CV), which is defined as the ratio of the standard deviation to the mean of the recombination rate distribution at five QWs. As the temperature was increased from 20 to 100°C, the CV of Rrad and RAuger decreased from 1.22 to 0.33 and from 1.63 to 0.38, respectively. Humphreys, “The ABC model of recombination reinterpreted: Impact on understanding carrier transport and efficiency droop in InGaN/GaN light emitting diodes,” J. The LED sample was operated under pulsed current injection with a pulse width of 0.5 ms and the duty cycle of 1% to minimize self-heating effects. Wang, Y. Werdell, “The SeaWIFS PAR product,” in Algorithm Updates for the Fourth SeaWIFS Data Reprocessing, NASA Technical Memorandum 2003-206892, S. (e) RMSE of k_1. Here, the effects of an inhomogeneous carrier distribution in MQWs on the IQE curve were included, and temperature-dependent redistribution of carriers in MQWs was also considered in simulations. Lu, S. The defocusing situation is simulated here, too. According to [24], its variance is $\hat {\sigma }_{n}^{2}=\sigma _{n}^{2}}\left ({8\pi \sigma _{g}^{4}}\right)$. The scatterplot labelled ‘ALL’ indicates combined observations from all test sites, plotted according to observation site (red to blue color scale). Yan, Z. Mueller-Mach, G. In this case, the effective active volume should be reduced significantly compared to the physical volume of MQWs [52–55]. Speck, “The efficiency challenge of nitride light-emitting diodes for lighting,” Phys. The QW numbers of 1 and 5 correspond to the QW nearest the n-GaN and the p-GaN layer, respectively. Juho, and H. Barros, T. [CrossRef] 31. Wei, “A global calibration method for multiple vision sensors based on multiple targets,” Meas. The chip dimension was 1 × 1 mm2. De Santi, M. Download Full Size | PPT Slide | PDF As displayed in Fig. 5, the RMSEs of different methods’ calibration results show a linear distribution, and no sharp rise occurs. Good agreements between the measured data and the IQE fit curves were observed up to 150 mA for all temperatures. In the analytical model, the carrier density was assumed to be constant through the MQWs independent of temperature. Learn more. Wang, L. The upper and lower sides of the rectangle represent 75% and 25% of the error, respectively. On the other hand, δ is dependent on the detailed band structures and the carrier density, resulting in a more complicated temperature dependence [41]. [CrossRef] 44. The proposed method breaks the limitations of depth of field and target size existing in current camera calibration methods. Luong, and S. Sabathil, B. Strassburg, I. [CrossRef] 32. Concurrently, OURS can determine the convolutional scale adaptively compared with GS, and thus, OURS performs better. 37, 855–866 (1971).21. [CrossRef] 19. Simulation and physical experiments validate the effectiveness of the proposed method.Camera calibration is an important part of vision measurement, because its accuracy determines that of measurement systems. Park, D. Theoretical studies showed weakly increasing behaviors in C with temperature, whereas experimental studies mostly reported that C in InGaN MQWs decreased with increasing temperature. For this purpose, many studies have investigated the temperature dependence of the recombination coefficients in InGaN quantum wells (QWs) [14–23].In general, the carrier recombination rate in QWs can be denoted as An + Bn2 + Cn3, where A, B, and C represent the Shockley–Read–Hall (SRH), radiative, and Auger recombination coefficients, respectively, and n is the carrier density in the QW active region. (Right) Comparison of large target and small target. ηp decreased from 0.655 to 0.555 as the temperature was increased from 20 to 100°C, which is quite similar to the results obtained using the analytical model in Fig. 2.Figure 6 plots the coefficients A and C used for the IQE fitting in Fig. 5 as a function of temperature. 6. Kuo, T. Cho, J. 114(7), 071101 (2013). On the other hand, inconsistent temperature-dependent trends in C have been reported in InGaN QWs. Theoretical studies have shown that C increases slowly with increasing temperature, corresponding to indirect Auger recombination processes [14–17]. Filled black triangles indicate values considered as outliers due to an extreme weather event experienced in the Yongala study site, which were excluded from the analysis (as previously reported). This descending behavior in the coefficient C with increasing T has also been demonstrated in several previous works [19–23]. [CrossRef] 28. Therefore, in this study, the theoretical formula of B will be used to obtain its temperature dependence. Karpov, A. These requirements cause difficulty in many calibration scenarios, such as those involving large-field-of-view, shallow-depth-of-field, or online operation cameras. With increasing temperature, Rrad and RAuger became homogeneous owing to thermally-enhanced hole transport. When the numerical simulation was employed to fit the EQE curve, C was found to increase by ~31% as the temperature was increased from 20 to 100°C. Wang [14] used Fourier transform to deal with defocus blur. For example, at a noise level of 0.1 pixel, noise with a standard deviation of 0.1 pixel is added to half of the feature points in one image, and that with 0.2 pixel is added to the other half of the points, to simulate that different points have different location variances. [CrossRef] Page 3 Corrections for equations in our recently published paper [Opt. [CrossRef] 12. It can be noticed that the area of the large target is more than 6 times that of the small target. Lett. Wu, X. Zhang, and A. Ryu, and H. Pattern Anal. In this way, the temperature dependence of A and C can be determined reliably using only the information of the theoretical temperature dependence of B.The coefficient B can be obtained from the spontaneous emission rate in QWs. The spontaneous emission rate at the angular frequency ω for the transition from the i state in the conduction band to the j state in the valence band is written as [9–11] (9)$${r_{sp}}(\omega) = \frac{{{n_r}{e^2}\omega }}{{\pi \hbar {c^3}{\varepsilon _0}m_0^2}}\sum\limits_{i,j} {\int_0^\infty {d{k_t}} (\frac{{{k_t}}}{{\pi {L_w}}})|{M_{ij}}({k_t})|^2}{f_i}(1 - {f_j})} ,$$ where nr, m0, kt, and Lw is the index of refraction, electron mass, in-plane wave vector, and thickness of a QW, respectively. Ambacher, “Evidence for nonlinear macroscopic polarization in III-V nitride alloy heterostructures,” Appl. Shortis, T. B 98(4), 779–789 (2010). Dalapati, N. On the other hand, when a numerical simulation was used to fit the measured EQE data, the temperature-dependent change in the carrier and recombination distribution was considered. [19–23] used InGaN/GaN MQW structures, whereas Ref. Chow, “Modeling of temperature and excitation dependences of efficiency in an InGaN light-emitting diode,” Opt. Wagner, M. [CrossRef] Previous Article Next Article View by: Article Order Year Author Publication M. The Mg doping concentration of the p-GaN and p-AlGaN layers was 1 × 1019 cm−3, and the Si doping concentration of the n-GaN layer was 5 × 1018 cm−3. Yang, Y. of IEEE International Conference on Computer Vision, (2015).26. Meyaard, Q. [CrossRef] 15. Wang, and X. Hasnain, “Modeling of GaN optoelectronic devices and strain-induced piezoelectric effects,” IEEE J. Kang, and B. Ko, T. (c) Relative RMSE of u_0. Lindeberg, “Feature detection with automatic scale selection,” Int. Because when camera is calibrated in the non-DoF range, image blur and noise vary from point to point, the standard deviations of different points are different. Chen, “Out-of-focus color camera calibration with one normal-sized color-coded pattern,” Opt. Quantum Electron. On the other hand, the hole concentration showed stronger temperature dependence. Ryu, D. Huang et al. Figure 7 shows the calibration scenarios of small target and large target, and compares areas of different size of targets. The calibration datasets are similar to those in Section 5.1, thus not displayed here. Grundmann, J. All kinds of targets are placed 20 times, and part of the calibration datasets are shown in Fig. 8. Peter, and B. Photonics 10(1), 246–308 (2018). Furthermore, this scale is defined as the best scale, $\sigma _{\tilde {g}}$, owing to its characteristics.In this study, a local reference frame, $o-st$, is established with the ideal location of the image feature point in the noiseless image as the origin, (0, 0), and the coordinate axes parallel to the u- and v-axes of the image reference frame as the coordinate axes. Ferreira, I. According to our experiments and experience, the targets are recommended to be placed at an angle of more than 20° to guarantee the calibration accuracy. Huang, H. Shchekin, and W. 80(7), 1204–1206 (2002). 44(13), 3254–3257 (2019). The accuracy of OURS is 12% higher than that of SZ for focal lengths and up to 22% higher for principal points and up to 20% higher for distortion coefficients. Kappers, R. This is also opposite to the results of other experimental studies on InGaN MQWs, where C decreased with temperature [19–23].The reason for these conflicting results on the temperature dependence of C is believed to be related to temperature-dependent distributions of the carrier density and recombination rate in MQWs. To address this aspect, we conducted simulations on carrier distribution and recombination rates in InGaN MQWs as the temperature was varied. Onwukaeme, “Efficiency droop and effective active volume in GaN-based light-emitting diodes grown on sapphire and silicon substrates,” Appl. X. 2. The measured EQE curve at each temperature will be used to fit the IQE using either the analytical model or numerical simulation.In this subsection, analytic expressions on the relationships between the carrier recombination coefficients were developed to determine the temperature dependence of C under a constant carrier density in MQWs. This procedure is basically similar to those reported elsewhere on the temperature-dependent recombination coefficients in InGaN QWs [18–23].In the ABC recombination model, the current, I, injected into active region is expressed as (2)$$I = qV(An + B{n^2} + C{n^3}),$$ where V is the active volume of MQW layers. [CrossRef] 33. The LED chip was fabricated as a vertical-injection structure by using wafer bonding and laser lift-off processes. Selection of calibration datasets. Wei and D. Concurrently, the error distributions of most calibration methods are the most concentrated when evaluated by IMG_MS, proving the high accuracy of the proposed adaptive multi-scale method. Wu, Z. Schaffer, B. W. [CrossRef] 13. In the experiments, cameras (AVT GT1920) with a resolution of 1936 pixel $\times$ 1456 pixel and a 23-mm Schneider’s lens are used. In case of defocus blur, the adaptive multi-scale method is used to extract feature point coordinates at first to ensure accuracy, and the location variance of each feature point is estimated concurrently. (Top) Large chessboard target. 20(2), 113–125 (1998). Mater. Oh, and J. Hahn, and J. Sabathil, J. Liu, G. Bhardwaj, J. Experiments verify the correctness of the model and the effectiveness of the normalized optimization method.3. The best scale ${{\sigma }_{{\tilde {g}}}}={{\sigma }_{w}}$ in the adaptive multi-scale extraction method is defined and proved. Experiments are repeated 100 times at each noise level, and noise is re-added each time to enhance the randomness of the experiment. In the non-depth-of-field range range, the proposed method is considerably superior to other methods, and its measurement accuracy is up to 0.0403%.2. In Fig. 9, average recombination rates in each QW for radiative and Auger recombination are plotted as a function of the QW number for temperatures from 20 to 100°C. (a) Scatterplots of concurrent log-transformed satellite-derived instantaneous benthic PAR (bPARi) and in situ bPAR at four test sites (Yongala, Heron, Palm Passage, and Myrmidon). Van de Walle, “Temperature and carrier-density dependence of Auger and radiative recombination in nitride optoelectronic devices,” New J. Van de Walle, “Indirect Auger recombination as a cause of efficiency droop in nitride light-emitting diodes,” Appl. Tandon, W. Once the temperature dependence of B is obtained, A and C at the temperature T can be determined using Eq. (6) as follows: (7)$$\frac{{A(T)}}{{A({T_0})}} = \left({\frac{{1 - {\eta_p}(T)}}{{1 - {n_p}({T_0})}}} \right)\sqrt {\frac{{{I_p}(T){\eta _p}({T_0})}}{{{I_p}({T_0}){\eta _p}(T)}}} \sqrt {\frac{{B(T)}}{{B({T_0})}}} $$ (8)$$\frac{{C(T)}}{{C({T_0})}} = \sqrt {\frac{{{I_p}({T_0}){\eta _p^3({T_0})}}}{{{I_p}(T){\eta _p^3(T)}}} \frac{{(1 - {\eta _p}(T))}}{{(1 - {\eta _p}({T_0}))}}\left[{\frac{{B(T)}}{{B({T_0})}}} \right]^{3/2}}$$ Here, T0 is the reference temperature. The accuracy of OURS is about 3 times that of SZ and 12.5% higher than that of GS. 11(2), 1600147 (2017). Speck, “Interwell carrier transport in InGaN/(In)GaN multiple quantum wells,” Appl. Piprek, “Comparative efficiency analysis of GaN-based light-emitting diodes and laser diodes,” Appl. The method has the following contributions and advantages:1. Status Solidi A 214(8), 1600826 (2017). (Left) Comparison of $\sigma _e$ and $Erms$. Choy, A. Thus, the half feature points near the camera are added with high-level noise and the other half are added with low-level noise. Therefore, C could decrease with increasing temperature as a result of an overestimation of C at low temperatures when the analytical ABC model with a constant carrier density was employed. [CrossRef] 21. [CrossRef] 3. 9.51. From the results in Fig. 2, the data set of np(T) and Ip(T) can be obtained for each temperature T.From Eq. (4), coefficients A and C are related to the coefficient B through ηp and Ip: (6)$$A = \sqrt {\frac{{{I_p}{{(1 - {\eta _p})}^2}}}{{4{\eta _p}qV}}} {B^{1/2}},\quad C = \sqrt {\frac{{qV{{(1 - {\eta _p})}^2}}}{{4{I_p}\eta _p^3}}} {B^{3/2}}.$$ Therefore, if the temperature dependence of one of the three coefficients is known, that of the remaining two coefficients can be determined from Eq. (6). These operators play two roles: 1) They can give the derivatives of the image and 2) they work as Gaussian kernels, which could recover the Gaussian distribution of the spot image from the saturated one or reshaped one.The normalized determinant of the Hessian matrix [23] is defined as C, which can be described as (7)$$C\left(u,v,{\sigma _{g}} \right)=\sigma _{g}^{4}\left({{\tilde{I}}_{uu}}\left(u,v \right){{\tilde{I}}_{vv}}\left(u,v \right)-\tilde{I}_{uv}^{2}\left(u,v \right) \right),$$ where $\sigma _g$ is the standard deviation of the Gaussian convolutional kernel.The standard deviation of the Gaussian distribution is defined as the scale. Schmidt, B. Kim, E. Ryu, and C. Chang, P. Steiauf, and C. Chen, and Y. Download Full Size | PPT Slide | PDF 5.2.1 Analysis of the evaluation results using target images in the DoF rangeThe evaluation target in this section is a light-spot target whose interval of adjacent points is 20 mm with a total of 6×6 feature points placed in the DoF range, and it is placed 9 times. Section 3 describes the detailed procedure of the proposed method. The coefficient A increased with increasing temperature as in the case of the analytical model in Fig. 4(a). For example, Douxchamps [16] designed a multi-ring disc target pattern, improving the location accuracy under defocus blur by increasing the area of the points. (a) relative RMSEs of f_x (b) relative RMSEs of f_y. Note that this correction also implies that all texts pertaining to Es or Es$(\lambda ,{0^ + })$, a nomenclature that could be misinterpreted as scalar irradiance, in the original manuscript should now read as $E_d^{{0^ + }}$or $E_d^{{0^ + }}(\lambda ,\theta {^{\prime}_{solz}}(\phi))$.In addition, the term inside the parenthesis in Eq. (13) is missing a negative sign [3] and should read as: (13)$${\phi _{rise}} = {\cos ^{ - 1}}{\bigg (}{ - \tan (\delta)\tan (lat)} {\bigg)}.$$We applied these corrections to our original benthic irradiance model and performed matchup and validation exercise as detailed in the original manuscript. Drechsel, R. Thus, $\sigma _g=\sigma _w$, which suggests that the location variance becomes the minimum concurrently. Kioupakis, P. Tsai, “A versatile camera calibration technique for high-accuracy 3d machine vision metrology using off-the-shelf tv camera and lenses,” IEEE J. Download Full Size | PPT Slide | PDF 5.1 Evaluation of intrinsic parameters calibrationOne camera is analyzed in the evaluation of the intrinsic parameters. Wu, S. Although high efficiencies have been achieved at relatively low current densities, GaN-based blue LEDs suffer from a significant decrease in efficiency as the current density is increased [4–7]. Thus, group (2) and (3) simulate this situation. Daniel, K. A. Song, “Implicit and explicit camera calibration: Theory and experiments,” IEEE Trans. Han, M. Kim, and J. Moloney, and S. Moreover, in this scenario, minimizing the re-projection error of each point without normalization in the optimization will lead to a sub-optimal solution.Therefore, the location variances estimated by the proposed model are used to normalize the re-projection error of each feature point to obtain the optimal solution. Figure 5 shows the simulated IQE curves that exhibited the best fit to the measured EQE data at temperatures of 20, 40, 60, 80, and 100°C. As the temperature was increased from 20 to 100°C, ηp decreased from 0.656 to 0.557. Chihara, “High-accuracy and robust localization of large control markers for geometric camera calibration,” IEEE Trans. De Santi, A. Zhang, N. Ryu, “Investigation of light extraction efficiency and internal quantum efficiency in high-power vertical blue light-emitting diode with 3.3 W output power,” Jpn. 6(5), 1600209 (2014). [CrossRef] 42. Therefore, the IQE fitting was performed up to 150 mA. Monnard, P. [CrossRef] 26. Moreover, $f.$ and $f..$ represent the values at (0, 0) in $o-st$ in the ideal image convoluted by the Gaussian first-order and second-order differential kernels, respectively, and $n.$ and $n..$ represent those of the image noise convoluted by the above two kernels.According to the characteristics of the Gaussian distribution, $f_s=f_t=0$, f_{ss}=f_{tt}, ${{f}_{st}}=0$, and n_{ss}